

**Najmul Abid**

Department of Mechanical Engineering,  
McGill University,  
817 Sherbrooke Street West,  
Montreal, QC, H3A 2K6, Canada  
e-mail: najmul.abid@mail.mcgill.ca

**Florent Hannard**

Department of Mechanical Engineering,  
McGill University,  
817 Sherbrooke Street West,  
Montreal, QC, H3A 2K6, Canada  
e-mail: florent.hannard@gmail.com

**J. William Pro**

Department of Mechanical Engineering,  
McGill University,  
817 Sherbrooke Street West,  
Montreal, QC, H3A 2K6, Canada  
e-mail: will.pro87@gmail.com

**Francois Barthelat<sup>1,2</sup>**

Department of Mechanical Engineering,  
McGill University,  
817 Sherbrooke Street West,  
Montreal, QC, H3A 2K6, Canada  
e-mail: francois.barthelat@colorado.edu

# Exploring the Fracture Toughness of Tessellated Materials With the Discrete-Element Method

*Architected materials contain highly controlled structures and morphological features at length scales intermediate between the microscale and the size of the component. In dense architected materials, stiff building blocks of well-defined size and shape are periodically arranged and bonded by weak but deformable interfaces. The interplay between the architecture of the materials and the interfaces between the blocks can be tailored to control the propagation of cracks while maintaining high stiffness. Interestingly, natural materials such as seashells, bones, or teeth make extensive use of this strategy. While their architecture can serve as inspiration for the design of new synthetic materials, a systematic exploration of architecture-property relationships in architected materials is still lacking. In this study, we used the discrete element method (DEM) to explore the fracture mechanics of several hundreds of 2D tessellations composed of rigid “tiles” bonded by weaker interfaces. We explored crack propagation and fracture toughness in Voronoi-based tessellations (to represent intergranular cracking in polycrystalline materials), tessellations based on regular polygons, and tessellations based on brick-and-mortar. We identified several toughening mechanisms including crack deflection, crack tortuosity, crack pinning, and process zone toughening. These models show that periodic architectures can achieve higher toughness when compared with random microstructures, the toughest architectures are also the most anisotropic, and tessellations based on brick and mortar are the toughest. These findings are size independent and can serve as initial guidelines in the development of new architected materials for toughness. [DOI: 10.1115/1.4044015]*

**Keywords:** discrete element modeling, tessellation, Voronoi, brick and mortar, toughness, fracture mechanics

## 1 Introduction

Specific microstructures, heterogeneities, or hybrid compositions are now widely used in modern materials to generate high performance [1]. These concepts are now pushed to the extreme with architected materials, which contain highly controlled structures and morphological features at length scales intermediate between the microscale and the size of the component. Architected materials include the now well-studied lattice materials, which contain only a small fraction of solid [2]. In contrast, the less-studied dense architected materials are fully solid and are made of building blocks of well-defined size and shape, arranged in two or three dimensions [3–5]. The building blocks are stiff so their deformation remains small and within elastic limits, but the interfaces between the blocks can channel cracks and undergo nonlinear deformations. Building blocks can therefore collectively slide, rotate, separate, or interlock, providing a wealth of tunable mechanisms and properties [5]. Material architecture can be used to combine high strength and toughness—two properties that are mutually exclusive in traditional engineering materials [6,7] or enhance impact resistance [8,9] and ballistic performance [10] in glasses or ceramics. Interestingly, nature is well ahead of engineers in making use of architected materials. Materials such as bone, teeth, or mollusk shells are also made of stiff building blocks of well-defined sizes and shapes, bonded together by deformable bio-adhesives. Material architectures exist in nature in a variety of size scales, from the micron-scale plates layer in nacre [11] and the cylindrical osteon in bones [12]

to the submillimeter mineralized tiles sheathing the cartilages of sharks [13] and the macroscale plates in turtle shells [14] (Fig. 1). The interplay between the shape, size, properties, and arrangement of the building blocks generates, together with non-linear behavior at the interfaces, powerful combinations of stiffness, strength, and toughness not yet found in synthetic materials [5,6,15]. The building blocks in natural materials do not only simply interact through contact and friction, but also through complex polymers with sacrificial bonds, dynamic crosslinks, and viscous behaviors [16,17]. The interplay of architecture and interfaces generates unique properties, for example, in mollusk shells or bone where stiffness and hardness are generated by high mineral contents, and toughness is generated by crack deflection [18,19], crack bridging [20], process zone toughening [11,21], or a combination of the above mechanisms [22,23].

Recent studies on architected materials and biological materials have therefore highlighted the potential of material architecture, but to this day, the lack of mechanistic models for dense architected materials makes optimization difficult and hinders the discovery of new designs. The exploration of new architectures can be performed using brute force optimization [24] or more recently using topological and geometrical optimization [25,26] or machine learning algorithms [27,28]. The majority of these studies are based on the finite element method, which becomes computationally prohibitive on large models that must capture nonlinear processes associated with crack propagation [29]. Recently, the discrete element method (DEM) was used to capture crack propagation and toughness in large models of nacre-like materials [29–31]. These models capture multiple toughening mechanisms that act together, some of them involving large volumes of material [29]. In this study, we extended this modeling approach to a wider range of tessellations that included Voronoi-based tessellations (representing typical polycrystalline materials where the intergranular fracture is dominant), tessellations based on regular polygons, and finally

<sup>1</sup>Corresponding author.

<sup>2</sup>Present address: Department of Mechanical Engineering, University of Colorado Boulder, 427 UCB, 1111 Engineering Dr, Boulder, CO 80309.

Contributed by the Applied Mechanics Division of ASME for publication in the JOURNAL OF APPLIED MECHANICS. Manuscript received April 2, 2019; final manuscript received May 30, 2019; published online June 13, 2019. Assoc. Editor: Thomas Siegmund.

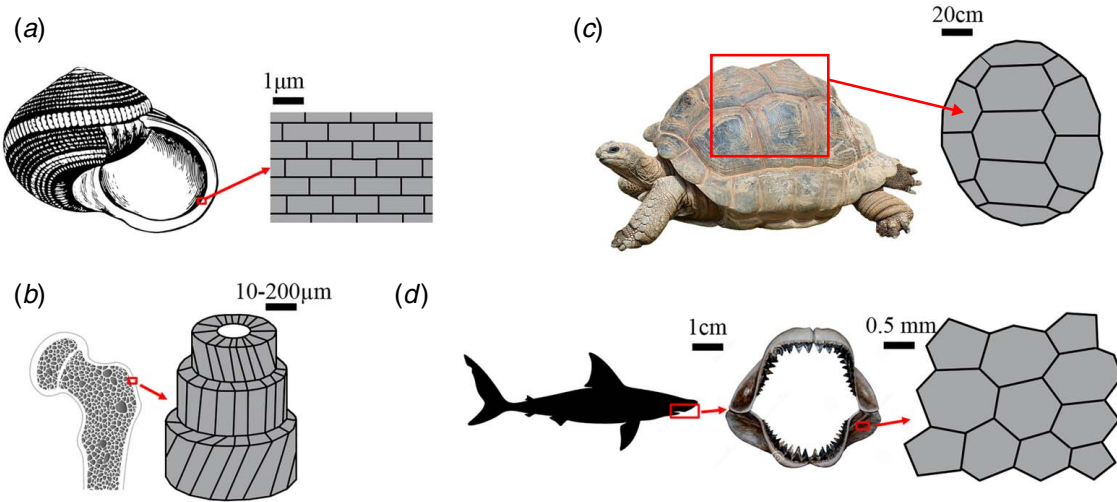


**Fig. 1** Examples of natural tessellations occurring in nature: (a) 3D brick and mortar tiling in nacre,<sup>3</sup> (b) cylindrical osteon in bones,<sup>4</sup> (c) plate-like geometry on turtle shells,<sup>5</sup> and (d) mineralized tesserae on the jaw of sharks<sup>6</sup>

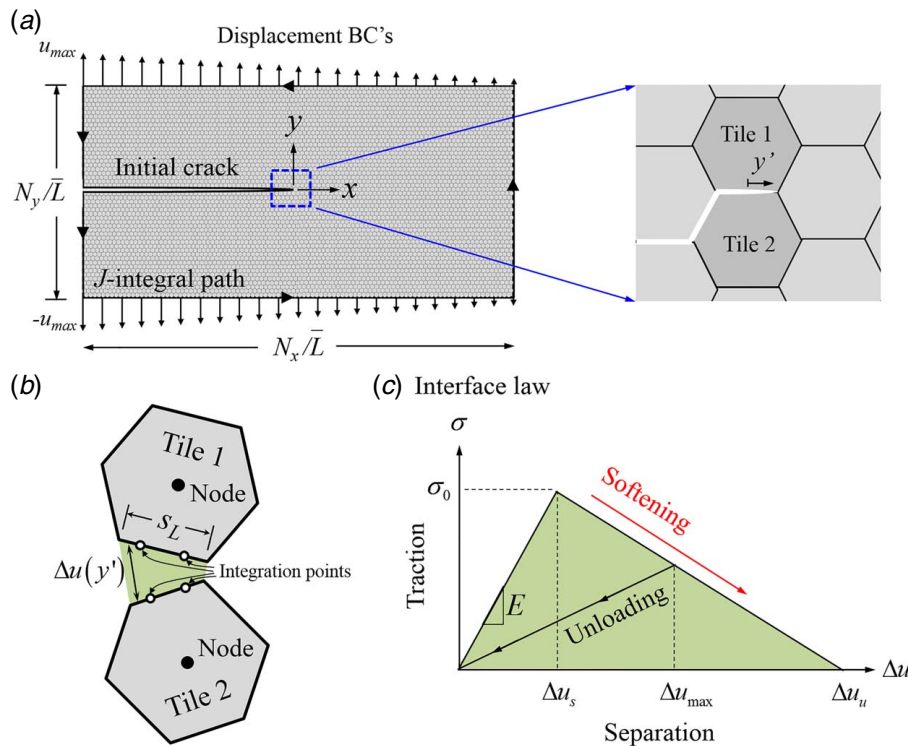


**Fig. 2** (a) Overview of the fracture DEM model showing full virtual specimen with dimensions, boundary conditions, and J-integral contour and close-up view of the rigid tile arrangement, (b) schematic of two rigid tiles with an interface in the deformed configuration, and (c) a triangular cohesive law that models the interactions between the two rigid tiles at the interface

tessellations based on brick and mortar tilings. More than a hundred tessellations were modeled, with crack propagation along five directions considered for each tessellation. The report concludes with an analysis of the results, which revealed recurrent failure patterns and design guidelines for 2D architected materials.

## 2 Fracture Model Setup and Validation

The fracture models we considered in this study are two-dimensional tessellations composed of rigid tiles (Fig. 2(a)), each tile being connected to its neighbors by nonlinear interfaces (Fig. 2(b)). The geometric effect of the interface thickness relative to the tile size is negligible and therefore is modeled with zero-thickness cohesive elements. The interface traction-displacement response is governed by a phenomenological cohesive law  $\sigma(\Delta u)$  which we assume to be triangular for simplicity (Fig. 2(c)). The interface separation  $\Delta u$  accounts for both the normal and tangential separation of the tiles caused by the translation, sliding, and rotation of the tiles (Fig. 2(b)) [32–34]. The initial slope is defined as  $E$

<sup>3</sup><https://www.freepng.es/png-63uj5u/>

<sup>4</sup><https://www.clipart.email/clipart/hip-bone-clipart-54841.html>

<sup>5</sup><https://pixabay.com/photos/turtle-tortoise-reptile-2815539/>

<sup>6</sup><http://www.amisvegetarian.com/shark-clipart-black-and-white-st-patricks-day-clipart/shark-clipart-black-and-white-great-white-shark-silhouette-at-getdrawings-free-for-personal-clipart-free-download/>

softening occurs when the interface separation exceeds  $\Delta u_s$ . The interface is considered broken (traction-free) once it reaches the critical separation  $\Delta u_u$ .

For this study, we set  $\Delta u_i/\Delta u_s = 15$  which gave a good resolution of the cohesive length. The cohesive secant stiffness  $k$  is defined as the ratio of the interface traction to the interface opening at any point:  $k = \sigma(\Delta u)/\Delta u$  ( $k = E$  in the elastic region). During unloading, the traction and the separation return to zero linearly with no residual deformation (i.e., damage model, Fig. 2(c)) and  $\Delta u_{\max}$  is the maximum separation experienced by the interface. The interface toughness defined as the area under the cohesive law in Fig. 2(c):

$$J_i = \frac{1}{2} \sigma_0 \Delta u_u \quad (1)$$

In the DEM approach, only the displacements and rotations of the center points of the tiles (nodes) are tracked as degrees of freedom, with three degrees of freedom per node in 2D. The interface opening displacement between adjacent tiles can be computed directly from the relative displacements and rotations of the tiles, since the tiles are assumed to be rigid. For the pair of tiles shown in Fig. 2(b), we denote the center point coordinates of tile 1 and tile 2 as  $(x_1^0, y_1^0)$  and  $(x_2^0, y_2^0)$ , respectively. The nodal displacements and rotations are represented in generic notation as  $q_1$ - $q_6$  where  $q_{3i-2}$  and  $q_{3i-1}$  are the translational displacements in the  $x$ - and  $y$ -directions (respectively) and  $q_{3i}$  is the rotational displacement of

tile “ $i$ ” ( $i = 1, 2$ ). For the deformed pair of the tiles shown in Fig. 2(b), the total interface opening separation  $\Delta u$  can be expressed in the undeformed interface coordinate system  $y'$  (Fig. 2(a)) as follows:

$$\Delta u(y') = \sqrt{(q_4 - q_1 + q_3(y' - y_1^0) + q_6(y_2^0 - y'))^2 + (q_5 - q_2 + x_1^0 q_3 - x_2^0 q_6)^2} \quad (2)$$

where the relative rotation between the two tiles was assumed to be small. In Eq. (2), the interface separation is computed from the relative translations and rotation of the tiles. This separation may involve opening displacements, shearing displacements, or a combination of the two. The stored elastic energy in the interface is computed as

$$W_{\text{int}} = \frac{1}{2} \int_{-s_L/2}^{s_L/2} \sigma(\Delta u(y'), \Delta u_{\max}) \Delta dy' \quad (3)$$

where  $s_L$  is the length of the interface and  $\sigma(\Delta u, \Delta u_{\max})$  is the internal interface traction with a damage variable denoted as  $\Delta u_{\max}$ . For computational efficiency, we used two-point Gauss quadrature ( $y' = \pm s_L/\sqrt{3}$ ) to perform the integral that gives

$W_{\text{int}}$

$$= \frac{s_L}{4} \left( (k_1 + k_2)(q_2 - q_5 - x_1^0 q_3 + x_2^0 q_6)^2 + \frac{1}{6} \left( k_1 \left( q_1 - q_4 + y_1^0 q_3 + \frac{s_L}{2\sqrt{3}}(q_3 - q_6) - y_2^0 q_6 \right)^2 + k_2 \left( q_1 - q_4 + y_1^0 q_3 + \sqrt{3}s_L(q_6 - q_3) - y_2^0 q_6 \right)^2 \right) \right) \quad (4)$$

where  $k_1$  and  $k_2$  are the cohesive secant stiffnesses (Fig. 2(b)) at the first and second integration points, respectively. The external work  $W_{\text{ext}}$  for the two-tile system is given as

$$W_{\text{ext}} = \sum_{i=1}^6 f_i q_i \quad (5)$$

where  $f_{3i-2}$  and  $f_{3i-1}$  are the forces and  $f_{3i}$  represents the moments on tile “ $i$ ” ( $i = 1, 2$ ). The total potential energy of the system  $W$  is simply given as

$$W = W_{\text{int}} - W_{\text{ext}} \quad (6)$$

The equilibrium configuration is governed by the minimum of potential energy:

$$\frac{\partial W}{\partial q_i}(q_1, f_1, q_2, f_2, \dots, q_n, f_n) = 0 \quad (7)$$

For the two-tile system shown in Fig. 2(b), Eq. (7) represents six ( $n = 6$ ) scalar equations and unknowns that can be regarded as either the forces or the displacements. Choosing the former, the solution is expressed as

$$\begin{aligned} f_1 &= g_1(q_1, q_2, \dots, q_n) \\ f_2 &= g_2(q_1, q_2, \dots, q_n) \\ &\dots \\ f_m &= g_m(q_1, q_2, \dots, q_n) \end{aligned} \quad (8)$$

where  $g_i$  are the generic nonlinear functions. To derive the components of the elemental stiffness matrix that defines an interaction between two tile centers, we set each DOF individually at unity

while fixing the other DOF's at zero [35]:

$$K_{ij}^e = g_i(q_1 = \delta_{ij}, q_2 = \delta_{2j}, \dots, q_n = \delta_{nj}) \quad (9)$$

where  $K_{ij}^e$  is the elemental DEM stiffness matrix and  $\delta_{ij}$  represents the Kronecker delta ( $\delta_{ij} = 1$  when  $i = j$  and  $\delta_{ij} = 0$  when  $i \neq j$ ). For completeness, the individual terms of the stiffness matrix are shown in Appendix for the DEM element in Fig. 2(b). In the linear region of the cohesive law,  $k_1 = E$  and  $k_2 = E$ , the elemental DEM equations are linear and expressed in a general form as

$$K_{ij}^e q_j = f_j \quad (10)$$

which can be assembled element-wise using standard procedures to form the global stiffness matrix. The element Jacobian entries are identical in the linear regime to the stiffness matrix entries  $J_{ij}^e = K_{ij}^e$ . In the nonlinear softening region, ( $\Delta > \Delta u_s$ ), the secant stiffness  $k$  is a nonlinear function of the element nodal degrees of freedom ( $k = \sigma(\Delta)/\Delta$ ), where  $\Delta$  is expressed in Eq. (2). In shorthand form, the nonlinear elemental DEM stiffness equation is expressed as

$$K_{ij}^e(q_1, q_2, \dots, q_n) q_j = f_j \quad (11)$$

The Jacobian entries in the softening regime are obtained through partial differentiation of Eq. (11):

$$J_{ij}^e = K_{ij}^e + \frac{\partial K_{ik}^e}{\partial q_j}(q_1, q_2, \dots, q_{12}) q_k \quad (12)$$

The elements were assembled, and the global response was computed using a DEM scheme that we implemented using MATLAB [36]. In the linear range, the nodal displacements and the rotations

are solved with a single function call to a standard sparse linear solver to solve Eq. (10)

$$\{q\} = [K] \setminus \{f\} \quad (13)$$

Once the system becomes nonlinear, Eq. (10) is solved with the classical Newton–Raphson (NR) method [37] with continuous stiffness and Jacobian updates in every NR iteration:

$$\{q\}_{z+1} = \{q\}_z - [J(q)] \setminus \{g(q)\} \quad (14)$$

where  $\{g(u)\}$  is the residual force vector that can be expressed as

$$\{g(q)\} = [K(q)]\{q\} - \{f\} \quad (15)$$

A time step was considered converged when the residual forces were less than  $10^{-4}$  N. After each converged load step, both the global stiffness matrix and the Jacobian matrix were updated based on the converged displacements. Interfaces that exceeded a separation  $\Delta u > \Delta u_u$  (cohesive traction vanishes) were considered fractured, and the fractured interfaces connected to the tip of the main crack contributed to crack advance. The position of the crack tip and the length of the crack were updated accordingly and at each time step. The effective crack length was determined at each time step as the projected length of the crack along the  $x$ -direction. The characteristic size of the tessellation was captured using  $\bar{L}$ , which is the average length of all the interfaces present in the model (Fig. 2(a)). The normalized size of the fracture model was then defined as  $N_x/\bar{L}$  by  $N_y/\bar{L}$ . A deep precrack was created in the model from the center of the left edge all the way to the center of the model (Fig. 2(a)), by removing the cohesive elements along the precrack (the length of the precrack was therefore always half of the horizontal width of the model (Fig. 2(a)). A linearly distributed displacement boundary conditions was applied on the upper and lower boundaries ( $y = \pm N_y/2\bar{L}$ ) of the model (Fig. 2(a)). The upper displacements followed the linear distribution:

$$u(x) = u_{\max} \left( \frac{1}{2} - \frac{x}{N_x/\bar{L}} \right) \quad (16)$$

where  $u_{\max}$  is the maximum displacement (at  $x = -N_x/2\bar{L}$ ). The lower boundary was subjected to the equivalent symmetric distribution. This particular distribution of displacement boundary conditions is consistent with applied rotations (bending) and promotes stable crack propagation in the system [31,38] in a way that is compliant with the Hill–Mandel condition [39]. Left and right boundaries ( $x = \pm N_x/2\bar{L}$ ) were free surfaces. During the simulation,  $u_{\max}$  was progressively increased to propagate a crack through the specimen. Stable crack propagation could be achieved in all simulations, as verified by numerical convergence for small incremental crack advances to a new stable equilibrium state as the loading was ramped.

At each loading step, the length of the crack was calculated automatically, and the crack driving force was computed using a discretized version of the  $J$ -integral [40]:

$$J = \int_{\Gamma} \left( W n_1 - t_i \frac{\partial u_i}{\partial x_1} \right) d\Gamma \quad (17)$$

where  $W$  is the strain energy density,  $n_1$  is the first component of the normal vector to the contour,  $t_i$  is the traction vector,  $u_i$  is the displacement vector, and  $\Gamma$  is the contour path. Because the top and the bottom edges of the integration contour were taken through the rigid tiles, and the integration contour of the other two edges (left and right) were taken through the interfaces, the  $J$ -integral (Eq. (17)) simplified to only include terms involving the strain energy density of the interfaces and the net reaction forces and displacements of the tiles on which the boundary conditions were applied. The  $J$ -integral is path independent if the  $J$  integration contour is taken far away from the crack tip, and if the plastic unloading is relatively small in comparison to the model size [41,42]. The  $J$ -integral contour we used here followed the outer edge of the model (Fig. 2(a)), and we made sure that a sufficiently large number of tiles was included in the models (large  $N_x/\bar{L}$  and  $N_y/\bar{L}$ ). For a given model size, we verified that different contours led to the same  $J$ -integral value (not shown here). The main outcome for each simulation was the crack resistance curve ( $R$ -curve) for a particular set of tessellations.

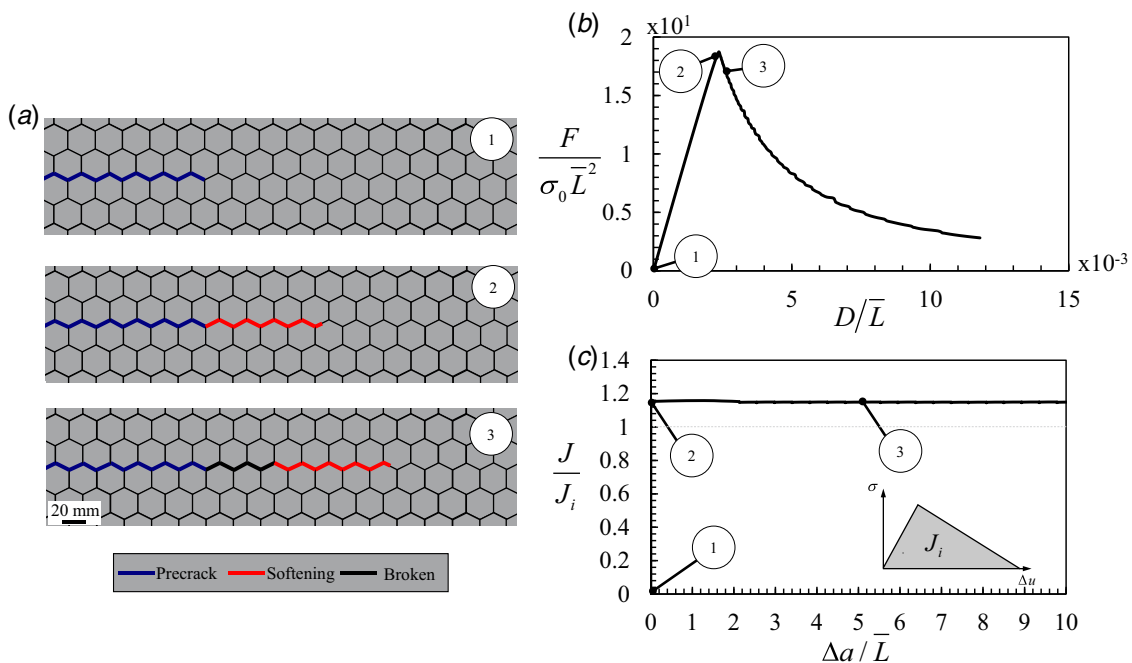


**Fig. 3** (a) Sequence of deformation and crack propagation in a hexagonal tessellation, (b) corresponding normalized force–displacement curve, and (c) corresponding crack resistance curve. The snapshots in (a) are magnified and only represent about 5% of the full model, which had full dimensions of  $N_x/\bar{L} = 52$  and  $N_y/\bar{L} = 181$ .

Figure 3 shows fracture simulation results from an example hexagonal tessellation. The evolution of the crack with increasing load is shown in Fig. 3(a). Initially, all interfaces deformed elastically until the highest stressed interfaces, just ahead of the crack tip, reached the yield strength  $\sigma_0$  and then immediately started to soften (shown in dark grey in Fig. 3(a)). As the applied displacement was increased further, more interfaces started to soften, forming a process zone ahead of the crack tip. Once the interface just ahead of the crack tip reached the critical separation  $\Delta u_m$ , the cohesive traction vanished and the crack propagated by a distance of one interface. Increasing the applied displacement further resulted in the stable propagation of the crack across the model (snapshot 3 in Fig. 3(a)). The corresponding normalized force–displacement curve (Fig. 3(b)) is qualitatively similar to what one would expect in a conventional fracture test with stable crack propagation [43]: Initial linear increase up to the onset of crack propagation, followed by a gradual decrease in the force as the crack propagates. The “softening tail” of the cohesive law was long enough (i.e., large  $\Delta U_m/\Delta U_s$ ) so we did not observe elastic snap-back during crack propagation. Therefore, numerical damping was not needed to achieve convergence [44]. The area under the force–displacement curve is related to the energy absorbed by the specimen, but the true fracture toughness is shown by the crack resistance curve in Fig. 3(c) which is the computed  $J$ -integral as a function of crack propagation.  $J$  progressively increases as the process zone develops and reaches a steady-state value when the crack started to propagate. Here, we normalize the toughness as  $J/J_i$  and the crack extension as  $\Delta a/\bar{L}$  where  $\Delta a$  is the crack length projected onto the  $x$ -direction. The crack resistance curve we obtained is size-independent because they are presented in normalized, dimensionless form. In addition, a fixed straight increment of crack propagation along the  $x$ -direction involves the fracture of a length of the interface that is dependent on the type of tiling but not on the size of the tiles. If the cohesive law at the interface is kept constant, then the size of the tiles has no effect on toughness. However, changing the size of the tiles for a fixed cohesive law would be equivalent to increasing the volume fraction of the tiles for a fixed interface thickness, with the effect of changing the stiffness of the tessellation: smaller tiles would lead to lower stiffness.

In the particular simulation shown in Fig. 3, the steady-state crack resistance is  $J/J_i = 1.13$ . For comparison, we derived the analytical solution based on the tortuosity of the crack path (the actual crack length divided by the shortest length from the start to the end of the crack) which gave us  $J/J_i = 1.15$ , within 2% of the prediction from the DEM simulation. Several other model validations with simple analytical models were performed but they are not shown here for brevity.

Before we present toughness predictions on a variety of tessellated materials in the next sections, we discuss some of the limitations of our DEM approach: (i) the details of crack propagation within individual interfaces are only captured approximately; therefore, the DEM models are appropriate only in cases when the process zone is larger than the size of individual tiles; (ii) our formulation assumes small relative rotations between tiles (for efficiency); therefore, we monitored the maximum relative rotation in the model, and in all cases, it was less than 3 deg, and finally, (iii) the model does not take into consideration the contact forces between the tiles (which would be computationally expensive). However, we monitored the interpenetration of the tiles during each simulation to ensure that it was negligible.

### 3 Voronoi Tessellation

The Voronoi tessellation has been used extensively in material science to represent polycrystalline microstructures with nonuniform grain shapes [45]. Indeed, the mathematical rules that govern a Voronoi tessellation are very similar to the physical rules governing the nucleation and growth of grains from a melt, with the location of the grain boundaries determined by the grain

growth velocities for the given seed pattern [45]. The construction of a Voronoi tessellation starts with a spatial distribution of points called seeds. A tessellation is then generated by dividing the plane into Voronoi cells, such that any point within each cell is closer to its seed than to any other seed [46]. Here, we used the DEM prediction for the “intergranular” fracture toughness of Voronoi tessellations as a reference value for a brittle two-dimensional polycrystalline material. We considered two types of Voronoi tessellations: random Voronoi tessellation (RVT) and centroidal Voronoi tessellation (CVT). The RVT is generated from a random distribution of seeds. This approach produces tessellation with overly large or small internal angles not observed in actual polycrystalline materials. CVT is a more realistic approach where a regularization step makes the seed points coincide with the centroids of individual Voronoi cells [47]. Here, we used the Lloyd algorithm that is one of the most popular iterative schemes for computing the CVTs [47]. It starts with an initial random distribution of seeds and consists of a simple iterative algorithm: (i) construct the Voronoi tessellation associated with the current seeds distribution, (ii) compute the centroid of each Voronoi polyhedron, and (iii) use these centroids as the seeds distribution to generate the Voronoi tessellation of the next iteration. The iterative procedure terminates when the seeds distributions between two consecutive steps meet some convergence criterion. The centroidal Voronoi tessellation results in more regular polygons containing less of these acute internal angles [48]. A total of 100 RVTs and 100 CVTs were generated and converted into a full DEM model. Each model contained 5000 Voronoi tiles and had a size of  $N_x/\bar{L} = 75$  by  $N_y/\bar{L} = 150$ . Figure 4 shows snapshots of the crack propagation together with a typical crack resistance curve produced by an RVT model. As expected, the crack broadly follows the direction of the driving force (from left to right), but the crack path is tortuous because of local crack deflection, a significant toughening mechanism due to the additional surface area traversed by a crack relative to the area of a straight path. In addition, high stresses “activate” the shortest (weakest) interfaces in a large region ahead of the crack tip, and this “cloud” of microcracks unloads when the crack advances (white interfaces in the wake of the crack). We also observed the formation of daughter cracks ahead of the main crack, as well as the formation of a few crack bridges behind the crack tip (Fig. 3(a), second snapshot). The crack propagation rate was not constant, and we observed multiple place where the crack is pinned into a tougher region. The applied load must be increased to unpin the crack and resume propagation. As a result, the crack resistance curve (Fig. 4(b)) is jagged and oscillates about  $J/J_i \sim 1.2$ .

Fracture simulation from a typical CVT model is shown in Fig. 4(a). The model contains more regular polygons compared with RVTs. The crack path is still tortuous because of repetitive local crack deflections but generally appears to be more straight at a larger scale compared with RVT. The process zone is more regular and more confined to the vicinity of the crack tip (the process zone size tends to decrease with increased uniformity of the tessellation) compared with RVT. Furthermore, crack bridging was never observed in the case of CVTs while it was frequently observed in the case of RVTs (see snapshot 2 of Fig. 4(a)). The crack resistance curve for CVT oscillates about a similar value when compared with RVT (i.e.,  $J/J_i \sim 1.2$ ) but the amplitude of these oscillations is clearly reduced.

In order to compare the fracture of RVTs and CVTs quantitatively, we computed the cumulative distribution function of all the normalized toughness ( $J/\bar{J}_i$ ) point across all 100 crack resistance curve in both cases (Fig. 5(a)). The resulting probability density functions (PDF) are shown in Fig. 5(b). The PDF for RVTs has a wider distribution compared with the taller and narrower PDF of CVTs. In other words, the variability in local toughness is greater for RVTs than for the CVTs. However, the average value, i.e., the center of symmetry of the PDF, remains very close the same value ( $J/\bar{J}_i = 1.21$ ) in both cases. The larger toughness variability of RVTs results from the more irregular tiles which

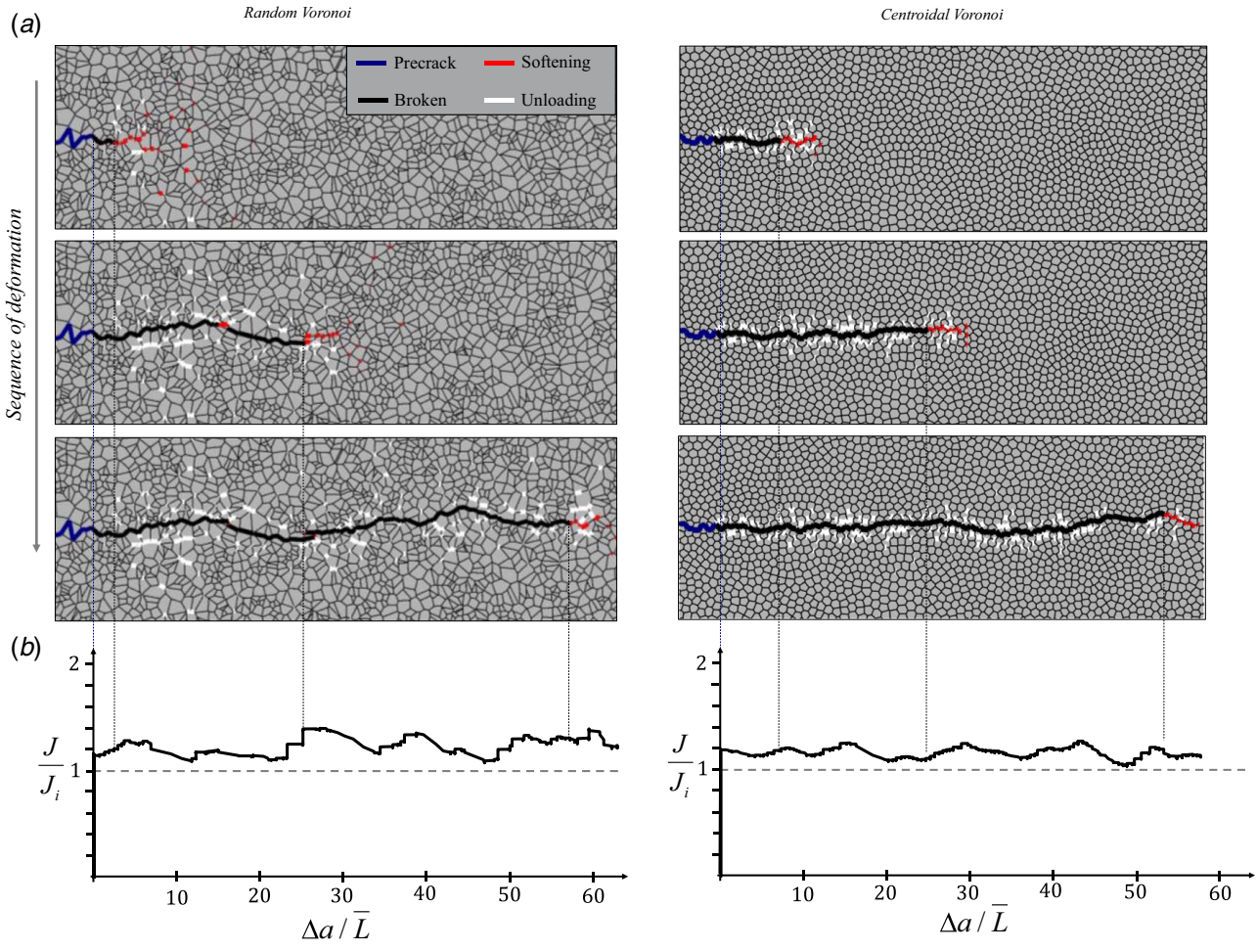


**Fig. 4 Typical fracture patterns in a Voronoi tessellation based on random and centroidal algorithms: (a) close-up of the crack propagation and (b) corresponding crack resistance curves**

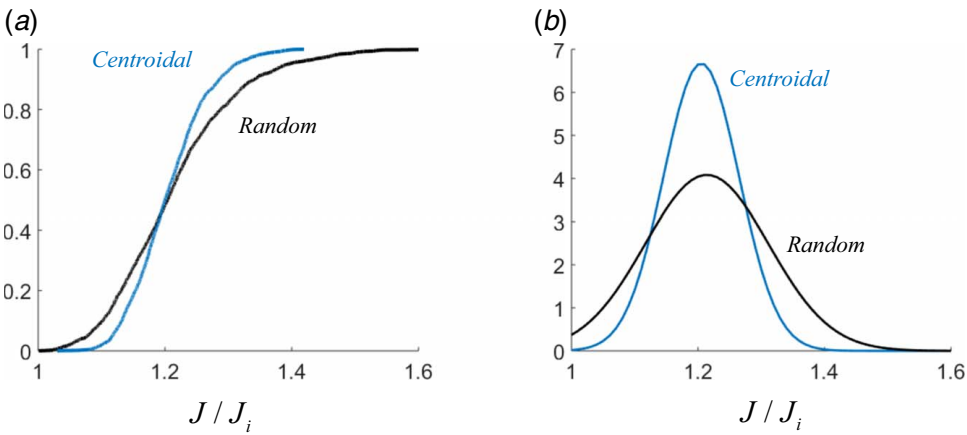


**Fig. 5 (a) Cumulative and (b) probability distribution of the normalized toughness for 100 random Voronoi tessellations and 100 centroidal Voronoi tessellations**

cause intermittent crack bridging and variations of the process zone size. However, since the average toughness is almost unchanged, crack deflection and tortuosity, present by an equal amount in the RVT and CVT models, are probably the main toughening mechanisms. Indeed, the average tortuosity (i.e., the actual crack length divided by the shortest distance between the start and the end of the crack) is equal to 1.2 in both cases. These results for the fracture toughness of “random” tessellations will serve as a reference for the

following sections that focus on architected, regularly tessellated materials.

**4 Tessellation With Regular Polygonal Tiles**

In this section, we explore periodic tessellations based on regular polygonal tiles to identify the toughest ones and to find out whether regular, “architected” tessellations are superior to random

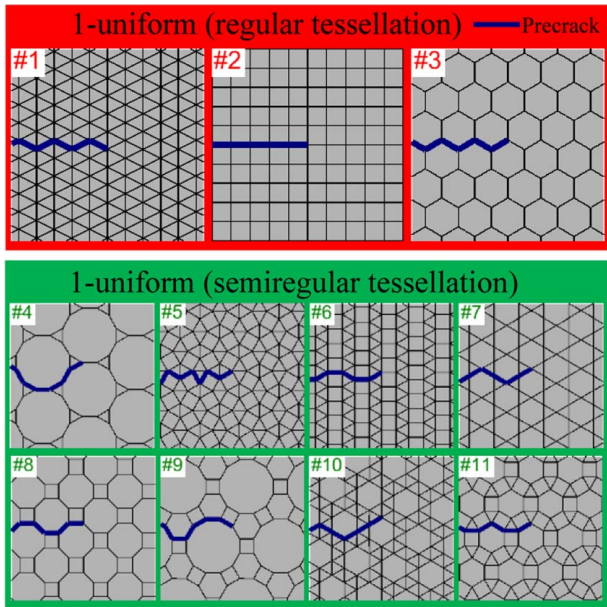


**Fig. 6** DEM models of the 11 1-uniform tessellations (regular tessellation in red, semiregular tessellation in green) with a precrack at 0-deg orientation

microstructures in terms of fracture toughness. There are several ways to classify periodic tessellations, and in this study, we chose a classification based on the works of Grünbaum and Shephard [49] because it suits itself to a progressive increase in geometrical complexity. In this classification, “ $n$ -uniform” tessellations are defined based on the number of vertices in a tessellation that can be mapped through symmetries (i.e., translation, rotation, and reflection). The complexity of the tessellation increases when  $n$  is increased, and in this study, we considered tessellations with  $n = 1, 2,$  and  $3$ . The “1-uniform” tessellations include the three regular

tessellations (Fig. 6) as well as semiregular tessellations which use two types of polygons (eight total tessellations; also known as uniform or Archimedean tessellation; Fig. 6). The “2-uniform” tessellations (20 total tessellations; Fig. 7), and “3-uniform” tessellation (61 total tessellations; Fig. 8) are all based on regular polygons with identical edge length  $L$  and equal internal angles. All tessellations considered in this section have an “edge-to-edge” arrangement where the edges of neighboring tessellations always fully overlap (non-edge-to-edge tessellations are discussed in Sec. 5). We implemented a MATLAB procedure to automatically generate large fracture models for each of the tessellations (Figs. 6–8). Since it is expected for the fracture toughness to be orientation-dependent, for each tessellation, we ran models with the initial crack and loading direction oriented at five different angles (0 deg, 30 deg, 45 deg, 60 deg, and 90 deg) relative to the initial tessellation geometries. We found that for some geometries, symmetrical crack bifurcations creates convergence issues. To alleviate this problem, we perturbed the strength of each interface in the model by a random  $\pm 0.01\%$ . These small perturbations did not have any effect on overall fracture toughness.

For each case, we used the same loading scenario shown in Fig. 2(a) and the  $J$ -integral was used as a measure of toughness. For each case, we also verified that the results were model-size independent. Figure 9(a) shows a typical set of results for crack propagation for a single tessellation tested along five directions, with corresponding crack resistance curves shown in Fig. 9(b). This particular tessellation (#43) is composed of triangles, squares, and hexagons. The average dimensions of these models were  $N_x/L = 54$  and  $N_y/L = 234$ . As expected, the toughness was generally higher than the toughness of the interface  $J_i$  due to crack tortuosity. In addition, crack propagation and toughness in this tessellation are anisotropic, and different orientations activated different mechanisms to produce different toughness (a common feature in architected materials [31,50]). The 90-deg orientation was the weakest and produced a toughness equal to the toughness of the interface because the crack was perfectly straight with no additional toughening mechanisms, while other orientation gave rise to crack deflection, crack tortuosity, pinning, and unpinning (which resulted in fluctuations on the crack resistance curves).

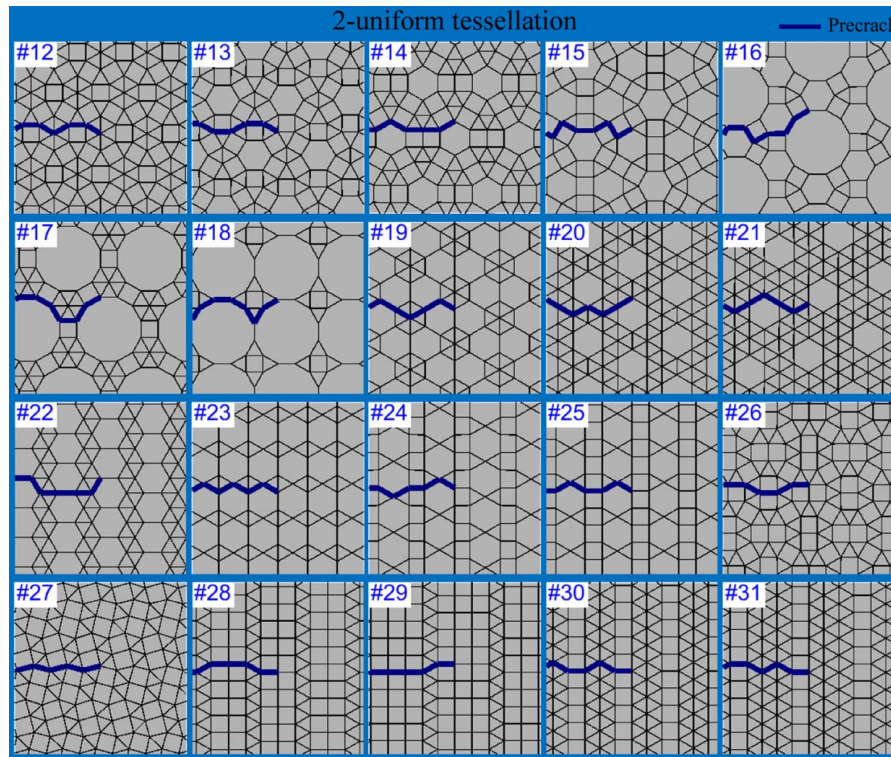


**Fig. 7** DEM models of the 20 2-uniform tessellation with a precrack at 0-deg orientation

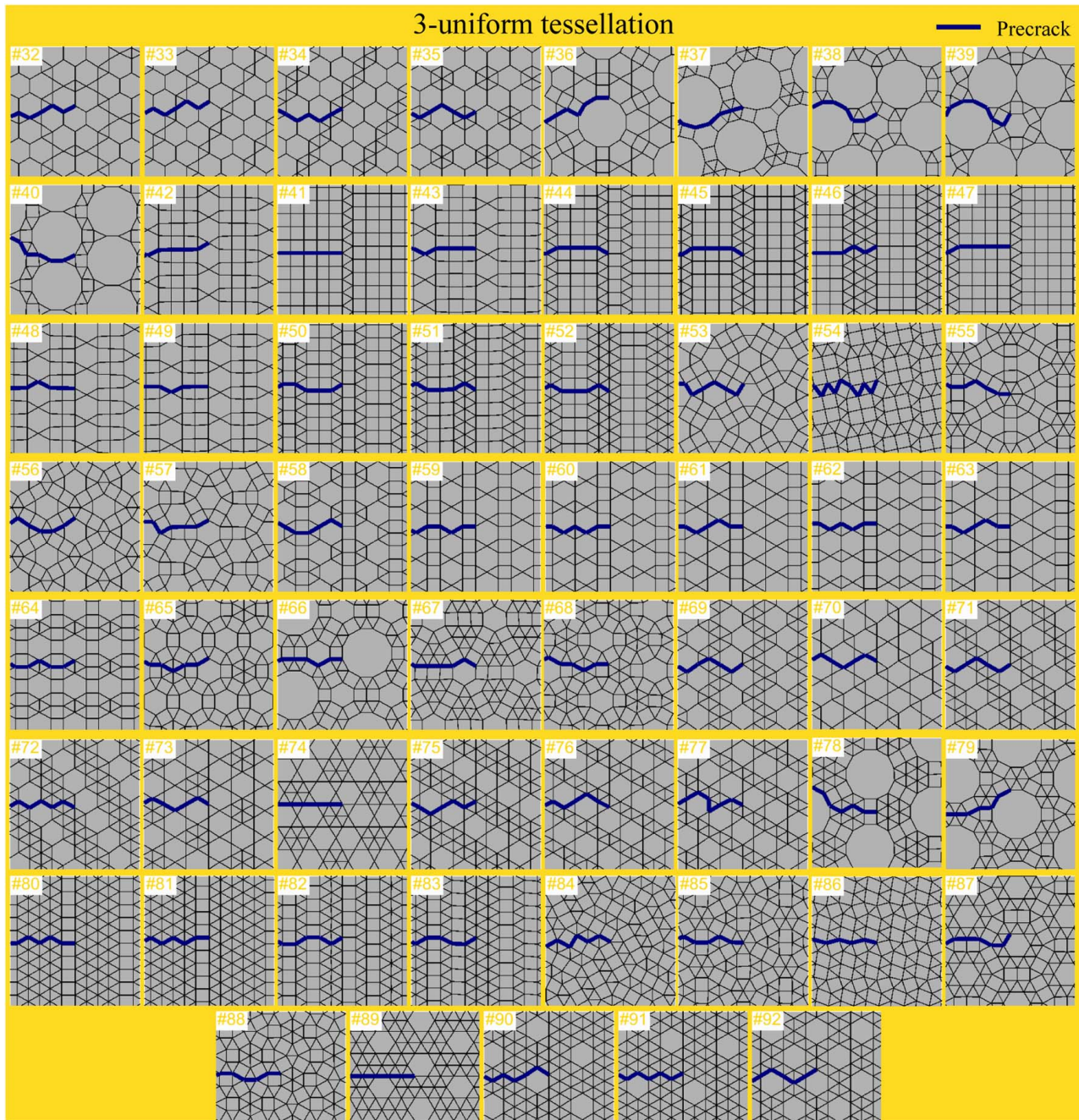


Fig. 8 DEM models of the 60 one 3-uniform tessellation with a precrack at 0-deg orientation

Interestingly, the 60-deg orientation also produced a rising crack resistance curve (Fig. 9(b)), because the crack propagated at an angle that required an increasing amount of driving force to unpin. Some of the orientations produced a small volumetric process zone (0 deg, 30 deg, 45 deg, and 60 deg orientations) while other orientations did not produce any (90-deg orientation in Fig. 9). The first reason for the formation of a process zone is  $t$ , the rotated orientation of the tiles at the crack tip, which activated yielding in one or both Gauss quadrature points in the surrounding interfaces (snapshot of 30-deg orientation in Fig. 9(b)). The second reason is due to the symmetry at the crack tip, which caused multiple yielding points just ahead of the crack tip (Snapshot of 45-deg orientation in Fig. 9(b)).

All tessellations produced fracture patterns and properties similar to case #43 (crack tortuosity, pinning-unpinning, and anisotropy). In order to compare and rank these tessellations, we sought a way to compute a single toughness value for each of the crack resistance

curves. This process can be done following ASTM standards [51,52], corrected beam theory, [53,54], curve fitting [55], or extracting the maximum, average, or minimum [56–58]. Most studies have used the last approach (maximum, average, or minimum), which is also the method we used here. In order to accommodate models with rising crack resistance curve behavior, we calculated the average normalized toughness  $\bar{J}/J_i$  over the first five cracked interfaces for all models as follows:

$$\frac{\bar{J}}{J_i} = \frac{1}{J_i(\Delta a/L)_5} \int_0^{(\Delta a/L)_5} J(\Delta a/L) d(\Delta a/L) \quad (18)$$

where  $(\Delta a/L)_5$  is the crack extension  $\Delta a/L$  at the fifth cracked interface. By this metric, the normalized average toughness for tessellation #43 is  $\bar{J}/J_i = 1.038$  at 0 deg,  $\bar{J}/J_i = 1.411$  at 45 deg, and  $\bar{J}/J_i = 1$  at 90 deg. We followed the same procedure for model

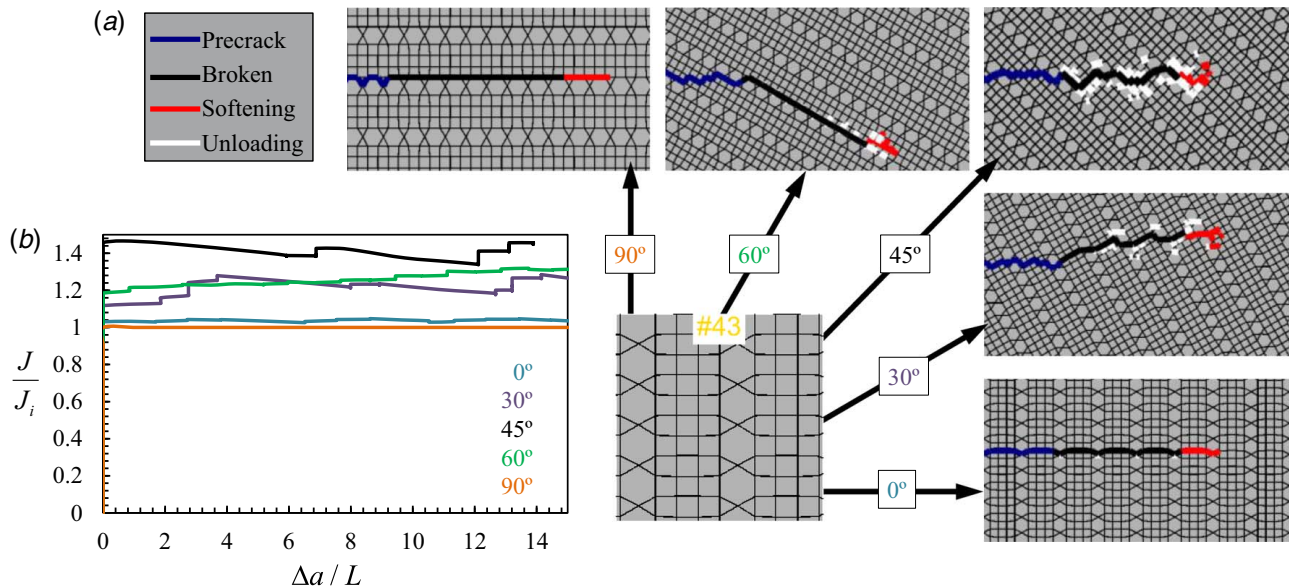


**Fig. 9 (a) Close-up snapshots for tessellation #43 with crack orientations at 0 deg, 30 deg, 45 deg, 60 deg, and 90 deg, and (b) corresponding crack resistance curves**

setup and analysis for all the 92 tessellations shown in Figs. 6–8. Figure 10(a) shows a summary of the results where the maximum average toughness  $\bar{J}_{\max}$  is plotted as a function of an anisotropy parameter which we defined as  $(\bar{J}_{\max} - \bar{J}_{\min})/\bar{J}_{\max}$ , where  $\bar{J}_{\max}$  and  $\bar{J}_{\min}$  are the maximum and minimum average toughness from the five orientations, respectively.

Figure 10(a) shows that, in general, the tessellation that produced the highest toughness was also the most anisotropic. The most isotropic (and weakest) tessellations are #32 and #55. Tessellation #32 had nearly the same crack paths in all direction. Tessellation #55's toughness is governed by tortuosity in the 0 deg and 60 deg orientations and pinning events due to symmetry in the 30 deg and 90 deg orientations (snapshot #55-90 deg in Fig. 10(c)). In terms of material design and selection, isotropy in toughness should be prioritized for applications where the state of stress is fluctuating or not known a priori. For these cases, tessellations #35, #36, and #38 offer useful combinations of isotropy and toughness in all directions. For other cases where the state of stress is well known, other tessellations should be selected and oriented to prevent failure along expected directions for crack propagation. In these cases, the tessellations with the highest toughness should be selected, even if they may be the most anisotropic. The most anisotropic tessellation is tessellation #2, which is the square tessellation (Fig. 10(a)). The weakest orientations for this particular tessellation are 0 deg and 90 deg, which result in a toughness equal to the toughness of the interface with a perfectly straight crack (snapshot #2-0 deg in Fig. 10(c)). The toughest orientation in the square tessellation is 45 deg, with a normalized average toughness of 1.527 due to a tortuous path and a process zone. We found that the toughest tessellation tested is #65 because two orientations (30 deg and 90 deg) promote crack branching (snapshot #65-30 deg in Fig. 10(c)). In addition to ranking the models by anisotropy and toughness, it is useful to identify recurrent toughening mechanisms. We found that in most tessellations, crack tortuosity was the main source of toughness. Here, we defined tortuosity as the total crack length divided by the shortest distance between the start and the end of the crack. Figure 10(b) shows the average normalized toughness (Eq. (18)) as a function of the tortuosity for all the DEM models. The majority of the models are clustered near a straight line with unit slope, which indicates that these models only rely on tortuosity for toughness. Tortuosity and crack deflection can produce relatively high toughness, but these tessellations produced very small process zones and lacked other toughening mechanisms such as crack

branching and bridging (snapshot of #2-0 deg and #10-45 deg in Fig. 10(c)). Tessellations that are far above the “tortuosity” line produced more powerful toughening mechanisms: in addition to crack deflection (snapshot of #47-45 deg in Fig. 10(c)): crack branching (snapshot #65-30 deg in Fig. 10(c)), crack pinning (snapshot #55-90 deg in Fig. 10(c)), and large volumes of process zone (snapshot #47-45 deg in Fig. 10(c)). Crack branching was observed with improvements in toughness when symmetry was composed of small polygons (number of sides  $<5$ ). Process zones developed because of two main factors. First, the rotation of the polygons at the crack tip initiated yielding in the surrounding interfaces (snapshot #65-30 deg in Fig. 10(c)) and second, a symmetry ahead of the crack tip yields interface to occur in both potential crack paths (snapshot #55-90 deg and #47-45 deg in Fig. 10(c)). Crack bridging was rarely observed in tessellations based on regular polygonal tiles.

## 5 Brick and Mortar Tessellations

The DEM models presented so far were all “edge-to-edge” type tessellations where edges of neighboring polygons fully overlapped. In this section, we explore other types of tessellations with only partial overlap. In order to restrict the design space to a manageable size, we chose to focus on non-edge-to-edge tessellation based on “brick and mortar” patterns, because this type of architecture is common in hard natural materials [59] and in bio-inspired architected materials [60]. We explored 19 unique arrangements of bricks adapted from Plummer [61] and developed the DEM models shown in Fig. 11. Some of the tessellations used only one brick geometry, while others used two brick geometries (long bricks with an aspect ratio of 5 and short bricks with an aspect ratio of 2.5).

Following the approach of Sec. 4, we considered five orientations for crack propagation for each of the 19 brick and mortar tessellation explored here. As an example, Fig. 12 shows the crack resistance curves and the corresponding close up snapshots of tessellation #99 for all the five different orientations. The average dimensions of these models were  $N_x/\bar{L} = 50$  and  $N_y/\bar{L} = 200$ . A dominant toughening mechanism observed with these types of tessellation is a large-scale crack deflection, crack pinning, and also in some cases the formation of a process zone. These mechanisms gave rise to high crack resistance (#99-0 deg in Fig. 12) when they operated simultaneously. Observation of the entire set of

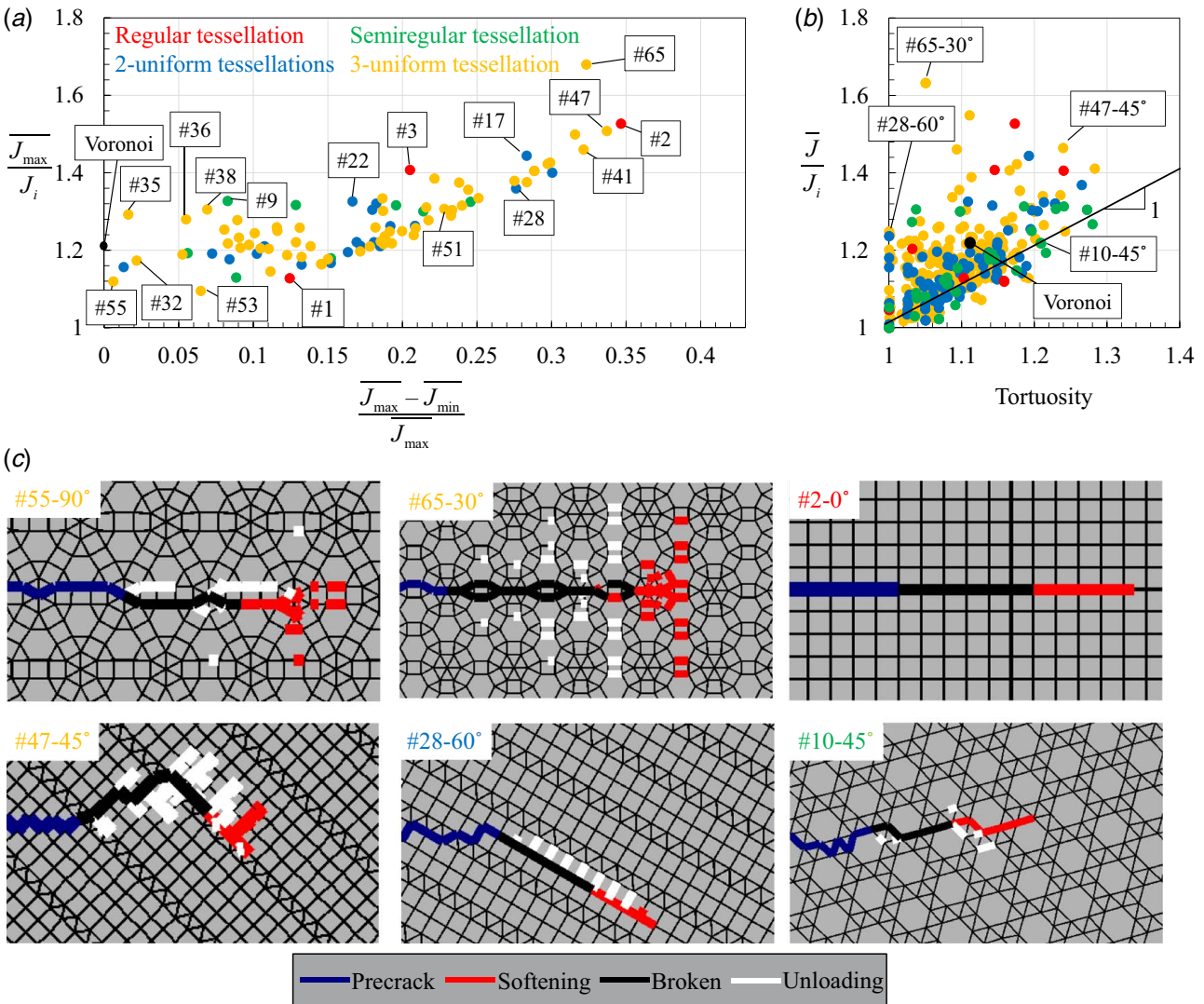


**Fig. 10 Summary of all the regular polygon-based tessellation: (a) maximum normalized toughness at any orientation as a function of anisotropic parameter, (b) average normalized toughness as function of crack tortuosity, and (c) selected close-up snapshots**

results for this type of tessellation revealed that the basic crack pinning and crack deflection mechanisms are generated by the partial overlapping of bricks. This arrangement generates a large number of “T-shaped” junctions that can pin incoming cracks. The aspect ratio of the bricks ahead of these junctions also influences toughness, with longer bricks creating larger obstacles. In addition, when the crack is pinned, the applied stresses must be increased to unpin the crack, and as a result, large process zones develop in the region of the pinning points (#99-0 deg orientation in Fig. 12(a)). These combined mechanisms produced the large amount of toughening.

We followed the same procedure for model setup and analysis for all 19 tessellations shown in Fig. 11. All tessellations in general produced fracture patterns that were similar to the example discussed above (crack tortuosity, pinning-unpinning, process zone, and anisotropy). Figure 13(a) shows a summary of the results for brick and mortar tessellation results, plotted with the results from the regular polygon tessellation for comparison. The brick and mortar tessellations are significantly more anisotropic but significantly tougher than the regular polygon-based tessellations and the Voronoi-based tessellations. This improvement is attributed to the large-scale crack deflection, strong pinning events, and large process zone that are the result of the arrangements of the bricks in a non-edge-to-edge formation. Crack branching was not observed

in the brick and mortar tessellations because of the strong presence of crack deflection in the 0-deg orientation, which gave preference to one crack path over the other and the lack of symmetry in the 30 deg, 45 deg, 60 deg, and 90 deg orientations. The toughest arrangement is #94 which also has the highest overlap area within bricks (snapshot #94-0 deg in Fig. 13(c)); surpassing #95 that has only half the overlap area as compared with #94 (Fig. 11). Figure 13(b) shows the average normalized toughness as a function of the tortuosity of all models explored in this report, polygon and brick and mortar tessellations. While some of the brick and mortar closely follow the guideline for the tortuosity-based toughness (Snapshot #110-45 deg in Fig. 13(c)), many other models are largely above this line, an indication that the toughening mechanisms discussed above can be very powerful in the brick and mortar tessellations (Snapshots #94-0 deg and #106-0 deg in Fig. 13(c)).

## 6 Summary

Tailoring microstructures to control crack propagation and increase toughness is a common strategy in materials design. In this work, we have explored the fracture mechanisms and fracture toughness of more than a hundred types of microstructures including typical “polycrystalline” structures based on Voronoi

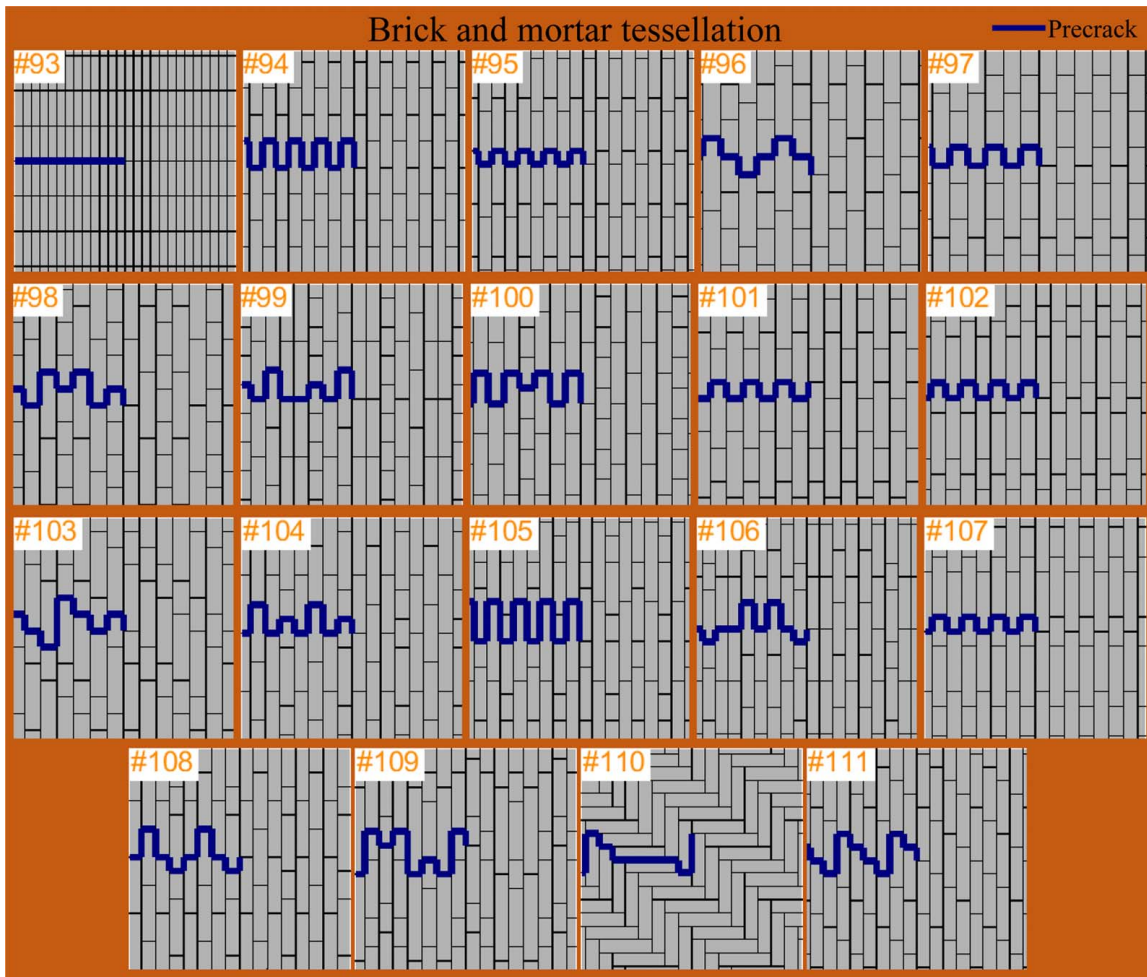


Fig. 11 Nineteen DEM models of brick and mortar tessellations shown with at 0-deg crack orientation. These snapshots are zoomed in at the crack tip.

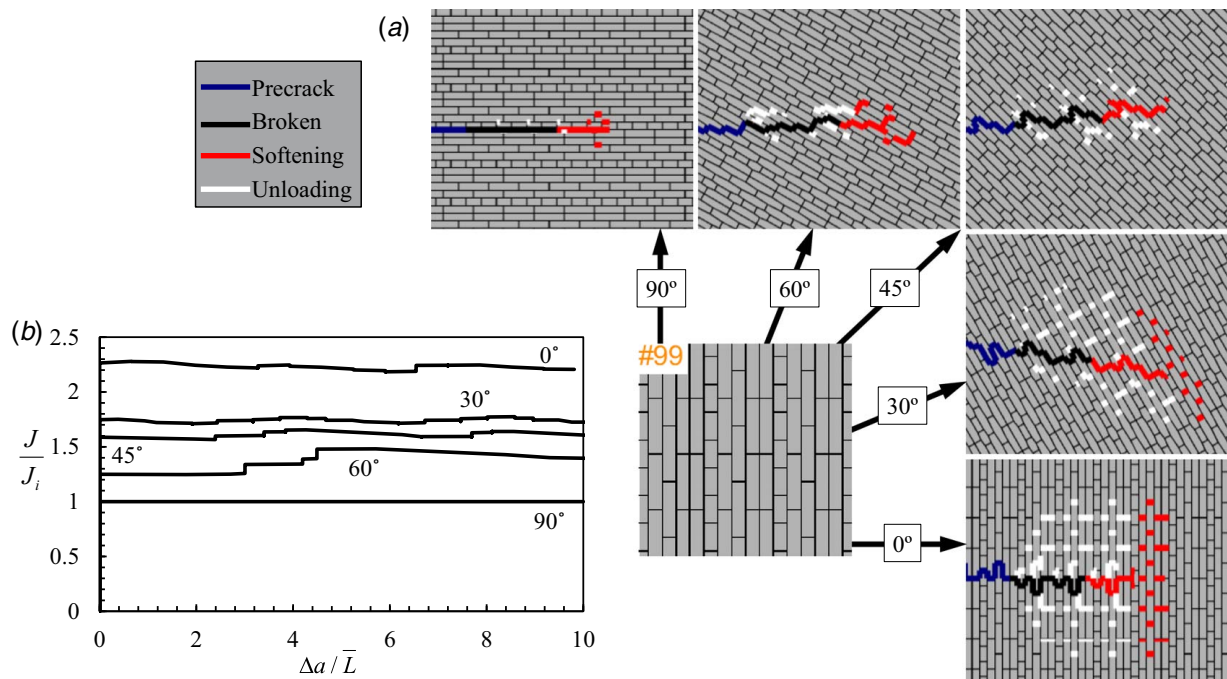
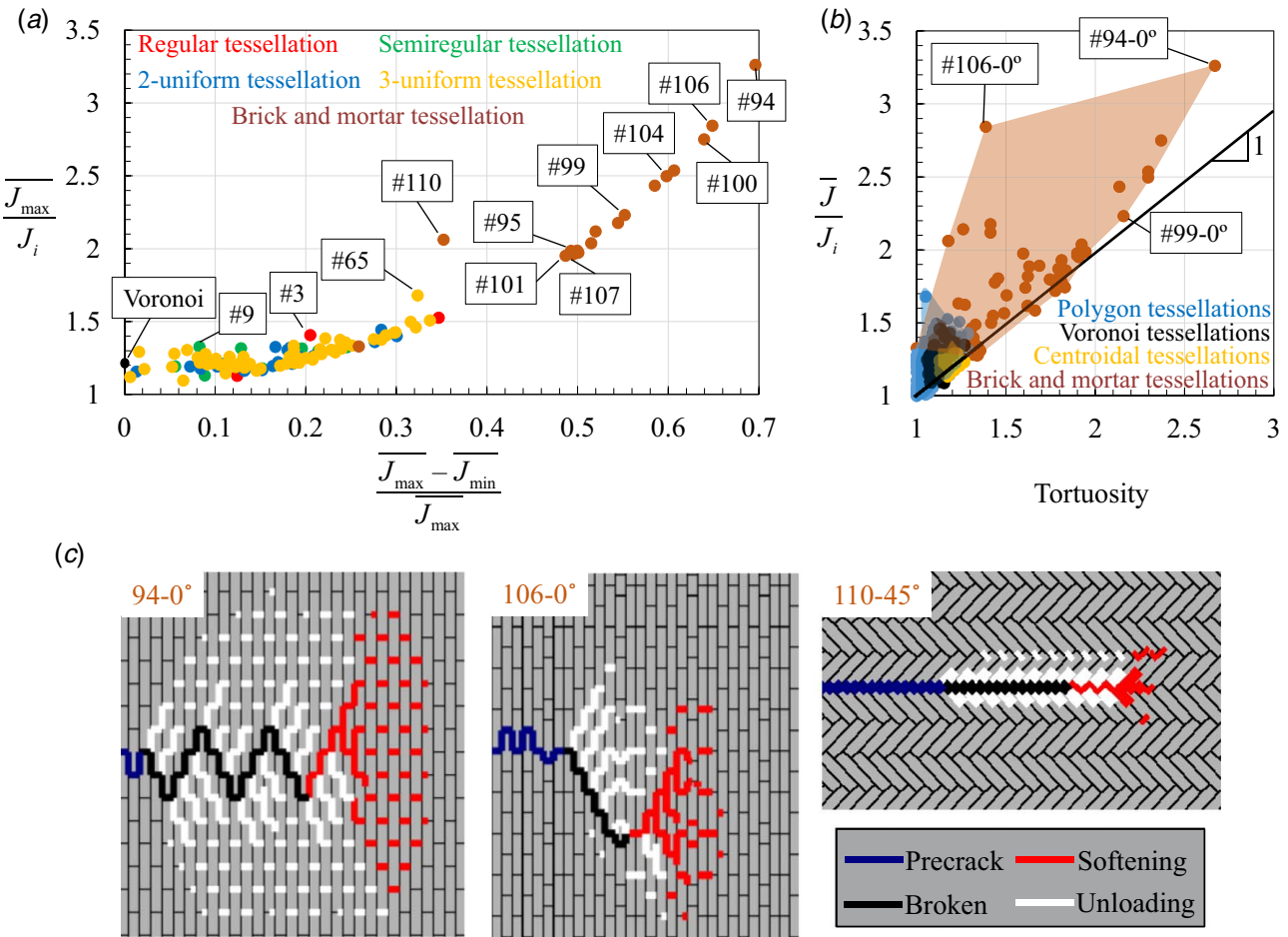


Fig. 12 (a) Close-up snapshots for tessellation #99 with crack orientations at 0 deg, 30 deg, 45 deg, 60 deg, and 90 deg and (b) corresponding crack resistance curves



**Fig. 13 Summary of all the tessellations explored in this report: (a) maximum normalized toughness at any orientation as a function of the anisotropic parameter, (b) average normalized toughness as a function of crack tortuosity, and (c) selected close-up snapshots of brick and mortar tessellations**

tessellations and “architected” materials based on periodic tessellations. For this study, we have used the discrete element method and assumed the tiles to be rigid, an assumption valid in the limit that the hard phase is much stiffer than the soft phase. This method is computationally efficient and enables the nonlinear modeling of crack propagation along five different directions for each of the structure. The main conclusions are as follows:

- (1) A wide range of fracture toughness and types of crack propagation was observed in the tessellations explored here. For most tessellations, crack tortuosity was the primary source of toughness. Other toughening mechanisms included crack branching, crack pinning and process zone toughening. Crack bridging was only observed in the Voronoi-based tessellations.
- (2) Higher toughness can be achieved in architected materials compared with regular Voronoi-based microstructures. The brick and mortar tessellations generated the highest toughness, followed by tessellations based on regular polygons. About half of the tessellations based on regular polygons were tougher than the Voronoi-based tessellations.
- (3) The most isotropic microstructures were the Voronoi-based tessellations. The most anisotropic structures were the brick and mortar tessellations. In general, the toughest architectures were the most anisotropic.
- (4) For the brick-and-mortar tessellation, toughness was higher for higher aspect ratio of the bricks. Toughness could be increased further by increasing the aspect ratio, up to the limit of brick fracture (which was not explored here).

- (5) Once a cohesive law is chosen for the interfaces, the toughening mechanism and toughness do not depend on the size of the tiles.

DEM is a powerful and computationally efficient method to model the fracture behavior of materials made of rigid tessellations with deformable interfaces. This method can capture several toughening mechanisms, which makes it a promising tool for the development of novel-architected materials optimized for toughness. DEM could also be a powerful tool to capture complex processes in various three-dimensional biological materials [59]. Finally, possible extensions of our approach include the fracture of three-dimensional architectures and the integration of the brute force exploration of the design space with more efficient optimization tools such as machine learning algorithms [27].

### Acknowledgment

This work was supported by a Strategic (Grant No. STPGP 479137-15) from the Natural Sciences and Engineering Research Council of Canada and by a Team (Grant No. 191270; Funder ID: 10.13039/501100000038) from the Fonds de Recherche du Québec—Nature et Technologies. N.A. was partially supported by a McGill Engineering Doctoral Award. Computations were made on the supercomputer Guillimin from McGill University, managed by Calcul Québec and Compute Canada. The operation of this supercomputer is funded by the Canada Foundation for Innovation (CFI) (Funder ID: 10.13039/501100000196), the Ministère de l’Économie, Science et innovation du Québec (MESI)

## Appendix

The full element stiffness matrix,  $K^e$ , for our DEM model is as follows:

$$K^e = \begin{bmatrix} \frac{1}{2}s_L & 0 & \frac{1}{12}s_L(6y_1^0\alpha + \sqrt{3}\alpha s_L) & -\frac{1}{2}\alpha s_L & 0 & -\frac{1}{12}s_L(6y_2^0\alpha + \sqrt{3}\beta s_L) \\ 0 & \frac{1}{2}\alpha s_L & -\frac{1}{2}x_1^0\alpha s_L & 0 & -\frac{1}{2}\alpha s_L & \frac{1}{2}y_1^0\alpha s_L \\ \frac{1}{12}s_L(6y_1^0\alpha + \sqrt{3}\alpha s_L) & -\frac{1}{2}x_1^0\alpha s_L & \frac{1}{24}s_L(12(x_1^0)^2 + (y_1^0)^2)\alpha + 4\sqrt{3}y_1^0\alpha s_L + \alpha s_L^2 & -\frac{1}{12}s_L(6y_1^0\alpha + \sqrt{3}\beta s_L) & \frac{1}{2}x_1^0\alpha s_L & \frac{1}{24}s_L(-12(x_1^0x_2^0 + y_1^0y_2^0)\alpha - 2\sqrt{3}(y_1^0 + y_2^0)\beta s_L + \alpha s_L^2) \\ -\frac{1}{2}\alpha s_L & 0 & -\frac{1}{12}s_L(6y_1^0\alpha + \sqrt{3}\alpha s_L) & \frac{1}{2}\alpha s_L & 0 & \frac{1}{12}s_L(6y_2^0\alpha + \sqrt{3}\beta s_L) \\ 0 & -\frac{1}{2}\alpha s_L & \frac{1}{2}x_1^0\alpha s_L & 0 & \frac{1}{2}\alpha s_L & -\frac{1}{2}x_2^0\alpha s_L \\ -\frac{1}{12}s_L(6y_1^0\alpha + \sqrt{3}\alpha s_L) & \frac{1}{2}x_2^0\alpha s_L & \frac{1}{24}s_L(-12(x_1^0x_2^0 + y_1^0y_2^0)\alpha - 2\sqrt{3}(y_1^0 + y_2^0)\alpha s_L + \alpha s_L^2) & \frac{1}{12}s_L(6y_2^0\alpha + \sqrt{3}\beta s_L) & -\frac{1}{2}x_2^0\alpha s_L & \frac{1}{24}s_L(-12(x_2^0)^2 + (y_2^0)^2)\alpha - 4\sqrt{3}y_2^0\beta s_L + \alpha s_L^2 \end{bmatrix}$$

where  $s_L$  is the interface length,  $\alpha = k_1 + k_2$ ,  $\beta = k_1 - k_2$ , and  $x_1^0$  and  $x_2^0$  are the  $x$ -coordinates of nodes 1 and 2, respectively, and  $y_1^0$  and  $y_2^0$  are the  $y$ -coordinates of nodes 1 and 2, respectively, in Fig. 2(b).

## References

[1] Ashby, M. F., 2005, "Hybrids to Fill Holes in Material Property Space," *Philos. Mag.*, **85**(26–27), pp. 3235–3257.

[2] Evans, A. G., Hutchinson, J. W., and Ashby, M. F., 1998, "Multifunctionality of Cellular Metal Systems," *Prog. Mater. Sci.*, **43**(3), pp. 171–221.

[3] Dyskin, A. V., Estrin, Y., Kanel-Belov, A. J., and Pasternak, E., 2001, "A New Concept in Design of Materials and Structures: Assemblies of Interlocked Tetrahedron-Shaped Elements," *Scr. Mater.*, **44**(12), pp. 2689–2694.

[4] Siegmund, T., Barthelat, F., Cipra, R., Habtour, E. M., and Riddick, J. C., 2016, "Manufacture and Mechanics of Topologically Interlocked Material Assemblies," *ASME Appl. Mech. Rev.*, **68**(4), p. 040803.

[5] Barthelat, F., 2015, "Architected Materials in Engineering and Biology: Fabrication, Structure, Mechanics and Performance," *Int. Mater. Rev.*, **60**(8), pp. 413–430.

[6] Ritchie, R. O., 2011, "The Conflicts Between Strength and Toughness," *Nat. Mater.*, **10**(11), pp. 817–822.

[7] Dyskin, A. V., Estrin, Y., Kanel-Belov, A. J., and Pasternak, E., 2001, "Toughening by Fragmentation—How Topology Helps," *Adv. Eng. Mater.*, **3**(11), pp. 885–888.

[8] Mirkhalaf, M., Tanguay, J., and Barthelat, F., 2016, "Carving 3D Architectures Within Glass: Exploring New Strategies to Transform the Mechanics and Performance of Materials," *Extreme Mech. Lett.*, **7**, pp. 104–113.

[9] Mirkhalaf, M., Zhou, T., and Barthelat, F., 2018, "Simultaneous Improvements of Strength and Toughness in Topologically Interlocked Ceramics," *Proc. Natl. Acad. Sci. U.S.A.*, **115**(37), pp. 9128–9133.

[10] Wadley, H. N. G., O'Masta, M. R., Dharmasena, K. P., Compton, B. G., Gamble, E. A., and Zok, F. W., 2013, "Effect of Core Topology on Projectile Penetration in Hybrid Aluminum/Alumina Sandwich Structures," *Int. J. Impact Eng.*, **62**, pp. 99–113.

[11] Barthelat, F., Tang, H., Zavattieri, P. D., Li, C.-M., and Espinosa, H. D., 2007, "On the Mechanics of Mother-of-Pearl: A key Feature in the Material Hierarchical Structure," *J. Mech. Phys. Solids*, **55**(2), pp. 306–337.

[12] Weiner, S., Traub, W., and Wagner, H. D., 1999, "Lamellar Bone: Structure–Function Relations," *J. Struct. Biol.*, **126**(3), pp. 241–255.

[13] Seidel, R., Lyons, K., Blumer, M., Zaslansky, P., Fratzl, P., Weaver, J. C., and Dean, M. N., 2016, "Ultrastructural and Developmental Features of the Tesselated Endoskeleton of Elasmobranchs (Sharks and Rays)," *J. Anat.*, **229**(5), pp. 681–702.

[14] Chen, I. H., Yang, W., and Meyers, M. A., 2015, "Leatherback Sea Turtle Shell: A Tough and Flexible Biological Design," *Acta Biomater.*, **28**, pp. 2–12.

[15] Wegst, U. G. K., Bai, H., Saiz, E., Tomsia, A. P., and Ritchie, R. O., 2015, "Bioinspired Structural Materials," *Nat. Mater.*, **14**(1), pp. 23–36.

[16] Barthelat, F., Yin, Z., and Buehler, M. J., 2016, "Structure and Mechanics of Interfaces in Biological Materials," *Nat. Rev. Mater.*, **1**(4), p. 16007.

[17] Dunlop, J. W. C., Weinkamer, R., and Fratzl, P., 2011, "Artful Interfaces Within Biological Materials," *Mater. Today*, **14**(3), pp. 70–78.

[18] Bajaj, D., and Arola, D. D., 2009, "On the R-Curve Behavior of Human Tooth Enamel," *Biomaterials*, **30**(23–24), pp. 4037–4046.

[19] Kamat, S., Su, X., Ballarini, R., and Heuer, A. H., 2000, "Structural Basis for the Fracture Toughness of the Shell of the Conch *Strombus Gigas*," *Nature*, **405**(6790), pp. 1036–1040.

[20] Koester, K. J., Ager J. W., III, and Ritchie, R. O., 2008, "The True Toughness of Human Cortical Bone Measured with Realistically Short Cracks," *Nat. Mater.*, **7**(8), pp. 672–677.

[21] Smith, B. L., Schäffer, T. E., Viani, M., Thompson, J. B., Frederick, N. A., Kindt, J., Belcher, A., Stucky, G. D., Morse, D. E., and Hansma, P. K., 1999, "Molecular Mechanistic Origin of the Toughness of Natural Adhesives, Fibres and Composites," *Nature*, **399**(6738), pp. 761–763.

[22] Fratzl, P., and Weinkamer, R., 2007, "Nature's Hierarchical Materials," *Prog. Mater. Sci.*, **52**(8), pp. 1263–1334.

[23] Sen, D., and Buehler, M., 2011, "Structural Hierarchies Define Toughness and Defect-Tolerance Despite Simple and Mechanically Inferior Brittle Building Blocks," *Sci. Rep.*, **1**(35), pp. 1–9.

[24] Barthelat, F., and Mirkhalaf, M., 2013, "The Quest for Stiff, Strong and Tough Hybrid Materials: An Exhaustive Exploration," *J. R. Soc. Interface*, **10**(89), p. 20130711.

[25] Gu, G. X., Wettermark, S., and Buehler, M. J., 2017, "Algorithm-driven Design of Fracture Resistant Composites Realized Through Additive Manufacturing," *Addit. Manuf.*, **17**, pp. 47–54.

[26] Gu, G. X., and Buehler, M. J., 2018, "Tunable Mechanical Properties Through Texture Control of Polycrystalline Additively Manufactured Materials Using Adjoint-Based Gradient Optimization," *Acta Mech.*, **229**(10), pp. 4033–4044.

[27] Gu, G. X., Chen, C.-T., and Buehler, M. J., 2018, "De Novo Composite Design Based on Machine Learning Algorithm," *Extreme Mech. Lett.*, **18**, pp. 19–28.

[28] Gu, G. X., Chen, C.-T., Richmond, D. J., and Buehler, M. J., 2018, "Bioinspired Hierarchical Composite Design Using Machine Learning: Simulation, Additive Manufacturing, and Experiment," *Mater. Horiz.*, **5**(5), pp. 939–945.

[29] Abid, N., Pro, J. W., and Barthelat, F., 2018, "Fracture Mechanics of Nacre-Like Materials Using Discrete-Element Models: Effects of Microstructure, Interfaces and Randomness," *J. Mech. Phys. Solids*, **124**, pp. 350–365.

[30] Abid, N., Mirkhalaf, M., and Barthelat, F., 2018, "Discrete-element Modeling of Nacre-Like Materials: Effects of Random Microstructures on Strain Localization and Mechanical Performance," *J. Mech. Phys. Solids*, **112**, pp. 385–402.

[31] Pro, J. W., Kwei Lim, R., Petzold, L. R., Utz, M., and Begley, M. R., 2015, "GPU-Based Simulations of Fracture in Idealized Brick and Mortar Composites," *J. Mech. Phys. Solids*, **80**, pp. 68–85.

[32] Rezaekhani, R., and Cusatis, G., 2016, "Asymptotic Expansion Homogenization of Discrete Fine-Scale Models With Rotational Degrees of Freedom for the Simulation of Quasi-Brittle Materials," *J. Mech. Phys. Solids*, **88**, pp. 320–345.

[33] Cusatis, G., and Schaffert, E., 2010, "Discontinuous Cell Method (DCM) for Cohesive Fracture Propagation," Proceedings of the 7th International Conference on Fracture Mechanics of Concrete and Concrete Structures (FramCos 7), Korea Concrete Institute, Seoul, May 23–28.

[34] Cusatis, G., Pelessone, D., and Mencarelli, A., 2011, "Lattice Discrete Particle Model (LDPM) for Failure Behavior of Concrete. I: Theory," *Cement Concrete Comp.*, **33**(9), pp. 881–890.

[35] Melosh, R. J., 1963, "Basis for Derivation of Matrices for the Direct Stiffness Method," *AIAA J.*, **1**(7), pp. 1631–1637.

[36] Mathews, J. H., and Fink, K. D., 2004, *Numerical Methods Using MATLAB*, Vol. 4, Pearson London, UK.

[37] Press, W. H., Teukolsky, S. A., Vetterling, W. T., and Flannery, B. P., 2007, *Numerical Recipes 3rd Edition: The Art of Scientific Computing*, Cambridge University Press, Cambridge, England/London/New York, p. 1256.

[38] Tada, H., Paris, P. C., and Irwin, G. R., 1973, *The Stress Analysis of Cracks*, Handbook, Del Research Corporation, Sandusky.

[39] Nguyen, V.-D., Béchet, E., Geuzaine, C., and Noels, L., 2012, "Imposing Periodic Boundary Condition on Arbitrary Meshes by Polynomial Interpolation," *Comput. Mater. Sci.*, **55**, pp. 390–406.

[40] Rice, J. R., 1968, "A Path Independent Integral and the Approximate Analysis of Strain Concentration by Notches and Cracks," *J. Appl. Mech.*, **35**(2), pp. 379–386.

[41] Kolednik, O., Schöngürndner, R., and Fischer, F., 2014, "A new View on J-Integrals in Elastic–Plastic Materials," *Int. J. Fract.*, **187**(1), pp. 77–107.

[42] Simha, N., Fischer, F. D., Shan, G. X., Chen, C. R., and Kolednik, O., 2008, "J-integral and Crack Driving Force in Elastic–Plastic Materials," *J. Mech. Phys. Solids*, **56**(9), pp. 2876–2895.

[43] Anderson, T. L., 2017, *Fracture Mechanics: Fundamentals and Applications*, CRC Press, Boca Raton, FL.

[44] Gao, Y., and Bower, A., 2004, "A Simple Technique for Avoiding Convergence Problems in Finite Element Simulations of Crack Nucleation and Growth on Cohesive Interfaces," *Modell. Simul. Mater. Sci. Eng.*, **12**(3), pp. 453.

[45] Zhang, P., Balint, D., and Lin, J., 2011, "An Integrated Scheme for Crystal Plasticity Analysis: Virtual Grain Structure Generation," *Comput. Mater. Sci.*, **50**(10), pp. 2854–2864.

- [46] Burger, G., Koken, E., Wilkinson, D. S., and Embury, J. D., 2013, "The Influence of Spatial Distributions on Metallurgical Processes," *Advances in Phase Transitions: Proceedings of the International Symposium Held at McMaster University Ontario, Canada, Oct. 22–23, 1987*, Elsevier, New York/Amsterdam.
- [47] Du, Q., Emelianenko, M., and Ju, L., 2006, "Convergence of the Lloyd Algorithm for Computing Centroidal Voronoi Tessellations," *SIAM J. Numer. Anal.*, **44**(1), pp. 102–119.
- [48] Alsayednoor, J., and Harrison, P., 2016, "Evaluating the Performance of Microstructure Generation Algorithms for 2-D Foam-Like Representative Volume Elements," *Mech. Mater.*, **98**, pp. 44–58.
- [49] Grünbaum, B., and Shephard, G. C., 1987, *Tilings and Patterns*, Freeman, San Francisco.
- [50] Keaveny, T. M., Morgan, E. F., Niebur, G. L., and Yeh, O. C., 2001, "Biomechanics of Trabecular Bone," *Annu. Rev. Biomed. Eng.*, **3**(1), pp. 307–333.
- [51] Srivastava, A., Ponson, L., Osovski, S., Bouchaud, E., Tvergaard, V., and Needleman, A., 2014, "Effect of Inclusion Density on Ductile Fracture Toughness and Roughness," *J. Mech. Phys. Solids*, **63**, pp. 62–79.
- [52] E1820-18a e1, A., "Standard Test Method for Measurement of Fracture Toughness," ASTM International.
- [53] Blackman, B., Dear, J. P., Kinloch, A. J., Macgillivray, H., Wang, Y., Williams, J. G., and Yayla, P., 1995, "The Failure of Fibre Composites and Adhesively Bonded Fibre Composites Under High Rates of Test," *J. Mater. Sci.*, **30**(23), pp. 5885–5900.
- [54] De Moraes, A., and Pereira, A., 2007, "Application of the Effective Crack Method to Mode I and Mode II Interlaminar Fracture of Carbon/Epoxy Unidirectional Laminates," *Composites, Part A*, **38**(3), pp. 785–794.
- [55] Heide-Jørgensen, S., de Freitas, S. T., and Budzik, M. K., 2018, "On the Fracture Behaviour of CFRP Bonded Joints Under Mode I Loading: Effect of Supporting Carrier and Interface Contamination," *Compos. Sci. Technol.*, **160**, pp. 97–110.
- [56] Hossain, M., Hsueh, C.-J., Bourdin, B., and Bhattacharya, K., 2014, "Effective Toughness of Heterogeneous Media," *J. Mech. Phys. Solids*, **71**, pp. 15–32.
- [57] Davidson, P., and Waas, A. M., 2012, "Non-smooth Mode I Fracture of Fibre-Reinforced Composites: an Experimental, Numerical and Analytical Study," *Phil. Trans. R. Soc. A*, **370**(1965), pp. 1942–1965.
- [58] Heide-Jørgensen, S., and Budzik, M. K., 2018, "Effects of Bondline Discontinuity During Growth of Interface Cracks Including Stability and Kinetic Considerations," *J. Mech. Phys. Solids*, **117**, pp. 1–21.
- [59] Naleway, S. E., Porter, M. M., McKittrick, J., and Meyers, M. A., 2015, "Structural Design Elements in Biological Materials: Application to Bioinspiration," *Adv. Mater.*, **27**(37), pp. 5455–5476.
- [60] Deville, S., Saiz, E., Nalla, R. K., and Tomsia, A. P., 2006, "Freezing as a Path to Build Complex Composites," *Science*, **311**(5760), pp. 515–518.
- [61] Plummer, H. C., 1950, *Brick and Tile Engineering: Handbook of Design*, Structural Clay Products Institute, Washington, DC.